



Universidad Autónoma  
de Madrid

**Biblos-e Archivo**  
Repositorio Institucional UAM

Repositorio Institucional de la Universidad Autónoma de Madrid  
<https://repositorio.uam.es>

Esta es la **versión de autor** del artículo publicado en:  
This is an **author produced version** of a paper published in:

Physical Chemistry Chemical Physics. 20.8 (2018): 5415-5426

DOI: <http://doi.org/10.1039/C7CP05307J>

**Copyright:** © Royal Society of Chemistry

El acceso a la versión del editor puede requerir la suscripción del recurso  
Access to the published version may require subscription

# Full dimensional potential energy surface and low temperature dynamics of the $\text{H}_2\text{CO} + \text{OH} \rightarrow \text{HCO} + \text{H}_2\text{O}$ reaction<sup>†</sup>

PCCP (2017), DOI: 10.1039/C7CP05307J

Alexandre Zanchet<sup>a</sup>, Pablo del Mazo<sup>a</sup>, Alfredo Aguado<sup>b</sup>, Octavio Roncero<sup>a</sup>, E. Jiménez<sup>c,d</sup>, André Canosa<sup>e</sup>, M. Agúndez<sup>f</sup> and J. Cernicharo<sup>f</sup>

A new method is proposed to represent analytically the potential energy surface of reactions involving polyatomic molecules capable to describe accurately long range interactions and saddle points, needed to describe low temperature collisions. It is based on two terms, a reactive force field term and a many body term. The reactive force field term describes accurately the fragments, long interactions among them and the saddle points for reactions. The many body term increase the desired accuracy everywhere else. This method has been applied to the  $\text{OH} + \text{H}_2\text{CO} \rightarrow \text{H}_2\text{O} + \text{HCO}$ , giving a barrier of 27.4 meV. The simulated classical rate constants with this potential are in good agreement with recent experimental results [ Ocaña *et al.*, *Astrophys. J.*, 2017, **submitted** ], **showing an important** increase for temperatures below 100K. The reaction mechanism is analyzed in detail here, and explains the observed behavior at low energy by the formation of long lived collision complexes, with roaming trajectories, with a capture observed for very long impact parameters,  $\sim 100$  a.u., determined by the long range dipole-dipole interaction.

## Introduction

Organic molecules have been widely detected in the interstellar medium (ISM), in hot cores, hot corinos, protoplanetary disks, etc<sup>1</sup>. Being among the largest stable molecules detected in space when these molecules have more than 6 atoms they are commonly called Complex Organic Molecules (COMs)<sup>2</sup>. The first organic molecules detected, and probably among the most abundant ones, are formaldehyde<sup>3</sup> and methanol<sup>4</sup>. Formaldehyde and methanol are efficiently formed by irradiation of  $\text{CO-H}_2$  mixture ices<sup>5,6</sup> and by successive hydrogenation of CO on dust grains<sup>7–10</sup>, while in gas phase many of the sequential steps present reaction barriers and are typically neglected<sup>11</sup>. At the colder regions at about 10K, these species can not thermally desorb, and they should pass to gas phase after absorbing high energy cos-

mic ray or UV radiation. Molecules like methanol, which forms very strong hydrogen bonds, are not easily desorbed by UV absorption, and instead they break and only the photofragments go to gas phase, as recently measured<sup>12,13</sup>. Therefore, if methanol is produced in ices, its photofragments once in gas phase can react to form back methanol<sup>13</sup>. Another possibility, is that methanol desorbs as a photofragment of a larger molecule still not found<sup>12</sup>.

The gas phase route to form COMs was recently opened by the measurement of a fast increase of the methanol with hydroxyl radical reaction rate constant at low temperature<sup>14</sup>, which was later confirmed by other experiments<sup>15,16</sup>. This gas phase reaction rate constant allowed to model properly the abundance of  $\text{CH}_3\text{O}$  radical observed in Barnard 1b<sup>16</sup>. The  $\text{CH}_3\text{OH} + \text{OH}$  reaction has two barriers of  $\sim 0.3$  and  $0.1$  eV, respectively, and the increase of the rate constant was explained by a tunneling mechanism within a transition state theory (TST) formalism<sup>14</sup>. The tunneling was estimated by calculating the imaginary frequency along the reaction coordinate at the saddle point for the reaction.

A recent study<sup>17</sup> has shown that this imaginary frequency was artificially too large, and that using a more realistic value yields too low reaction rate constants. Siebrand and co-workers also proposed an alternative model, in which a methanol dimer is formed which when colliding with OH gives rise to a  $\text{OH-CH}_3\text{OH}$  complex at energies below the  $\text{OH} + \text{CH}_3\text{OH}$  reactants threshold, so that it can only decay towards products by tunneling through the reaction barriers. This model was based on quasi-classical

<sup>a</sup> Instituto de Física Fundamental, Consejo Superior de Investigaciones Científicas, c/ Serrano 123, 28006 Madrid, Spain.

<sup>b</sup> Departamento de Química Física Aplicada, Unidad Asociada IFF-CSIC, Facultad de Ciencias C-XIV, Universidad Autónoma de Madrid, 28049 Madrid, Spain.

<sup>c</sup> Departamento de Química Física, Facultad de Ciencias y Tecnologías Químicas, Universidad de Castilla La Mancha, Avda. Camilo José Cela 1B, 13071 Ciudad Real, Spain.

<sup>d</sup> Instituto de Investigación en Combustión y Contaminación Atmosférica, Universidad de Castilla La Mancha, Camino de Moledores s/n, 13071 Ciudad Real, Spain.

<sup>e</sup> Institut de Physique de Rennes, UMR 6251 CNRS-Université de Rennes I, Campus de Beaulieu, Bât 11C, 263 Av. Général Leclerc, 35042, Rennes, France.

<sup>f</sup> Instituto de Ciencias de Materiales, Consejo Superior de Investigaciones Científicas, c/ Sor Juana de Inés de la Cruz, 3, 28049 Cantoblanco, Madrid, Spain.

E-mail: octavio.roncero@csic.es

trajectory (QCT) simulations for the complex formation rate constants and TST with tunneling for the reaction probability. In their calculation, Siebrandt et al. assumed a proportion of methanol dimers of 0.3 in the experiments<sup>14–16</sup>. A recent analysis by Shannon et al.<sup>18</sup> showed that this proportion is at most one order of magnitude lower at the lowest studied temperature, 50 K.

In order to solve this apparent problem, further experimental studies are needed to address the probability of complex forming, which in the model of Siebrand and co-workers<sup>17</sup> seems to be too high. In the experiments of Shannon and co-workers<sup>14</sup> the CH<sub>3</sub>O product was measured, appearing at a similar rate as the disappearance of the OH reactant. However, it is difficult to experimentally determine quantitatively the branching ratio to assess that the measured rate constant is completely assigned to the formation of CH<sub>3</sub>O products. For this reason, realistic theoretical simulations are convenient to unravel this dichotomy, beyond the TST models with tunneling made until now, describing the full reaction dynamics.

Recently, the reaction rate constant of formaldehyde with hydroxyl radical was measured below 100 K using the CRESU technique<sup>19</sup>. As in the case of methanol, the reaction rate constant shows an important increase with decreasing temperature. These rate constants were used to model the formation of HCO in different astrophysical environments, with a modest impact, since there are many other routes to form this molecule. The fast increase of the rate constant with decreasing temperature was well reproduced by QCT calculations based on an accurate potential energy surface (PES). The aim of this work is to show the method developed to generate such PES and to discuss the low temperature reaction dynamics to understand the interesting rise of the rate constant in this regime.

The paper is organized as follows. First, in section II, the method used to calculate the PES and represent it by analytic functions is described. Section III is devoted to show and discuss the QCT dynamical results, and finally in section IV some conclusions are extracted.

## Potential energy surface

### Ab initio calculations

The H<sub>2</sub>CO + OH → HCO + H<sub>2</sub>O reaction involves the OH(<sup>2</sup>) radical and for its description a multiconfigurational method is required. The spin-orbit splitting between the <sup>2</sup><sub>3/2</sub> and <sup>2</sup><sub>1/2</sub>, of 17.3 meV, is not taken into account in the electronic state calculation. The <sup>2</sup> state of OH is doubly degenerate (without including spin-orbit couplings). The ground and first excited states of H<sub>2</sub>CO + OH have been calculated at CASPT2 level, in order to determine if the first excited state may yield to products. The first excited state correlates with products in the excited HCO(<sup>1</sup>Σ<sup>+</sup>) state, which correlates with CO(a<sup>3</sup>). This state has been well characterized<sup>20</sup> and it has a linear equilibrium geometry, while the ground HCO(X<sup>2</sup>Σ<sup>+</sup>) is bent (with an equilibrium angle close to the HCO angle in H<sub>2</sub>CO). As a result, the saddle point for the excited electronic state is much higher (1 eV) than that of the ground electronic state. For this reason here we shall only consider the ground

### electronic state to study this reaction.

There are several previous *ab initio* calculations of the stationary points for the ground electronic state for this reaction<sup>21–24</sup>, shown in Table 1. These works use different methods to optimize the geometry and/or to calculate the harmonic zero-point energy (ZPE). The barrier height including ZPE vary between them, from -5.2 meV to 173 meV, but all the energies without ZPE are always positive.

**Table 1** Stationary points and Zero Point Energies calculated using RCCSD(T)-F12a method in this work and comparison with previous results (with the basis set used in parenthesis). All energies are in meV relative to the reactants in their equilibrium configuration. In the E+ZPE column, the quantity in parenthesis corresponds to the energy of reactants including ZPE.

Method	Energy	ZPE	E+ZPE
<b>H<sub>2</sub>CO+OH</b>			
This work VDZ-F12	0.0	957.0	957.0 (0.0)
CCSD(T) <sup>24</sup> aug-cc-pVTZ	0.0	954.0	954.0 (0.0)
MP4 <sup>23</sup> 6-311++G(3df,3pd)	0.0	971.5	971.5 (0.0)
MP2 <sup>22</sup> aug-cc-pVDZ	0.0	960.9	960.9 (0.0)
<b>H<sub>2</sub>CO OH</b>			
This work	-235.8	1045.8	810.0 (-147.0)
CCSD(T) <sup>24</sup>	-244.2	1041.3	797.1 (-156.9)
MP4 <sup>23</sup>	-157.8	1042.5	884.7 (-86.8)
MP2 <sup>22</sup>	-227.0	1041.8	814.8 (-146.1)
<b>Saddle point</b>			
This work	27.1	949.4	976.5 (19.5)
CCSD(T) <sup>24</sup>	24.10 <sup>-2</sup>	948.8	948.8 (-5.2)
MP4 <sup>23</sup>	70.1	932.4	1003.1 (31.6)
MP2 <sup>22</sup>	203.1	930.9	1134.0 (173.1)
<b>HCO H<sub>2</sub>O</b>			
This work	-1420.1	973.4	-446.7 (-1403.7)
CCSD(T) <sup>24</sup>	–	–	– (–)
MP4 <sup>23</sup>	-1450.3	1028.7	-421.7 (-1393.2)
MP2 <sup>22</sup>	-1582.6	983.7	-598.9 (-1559.8)
<b>HCO+H<sub>2</sub>O</b>			
This work	-1301.1	937.9	-363.3 (-1320.3)
CCSD(T) <sup>24</sup>	-1260.6	934.3	-326.3 (-1280.3)
MP4 <sup>23</sup>	-1387.7	950.6	-437.1 (-1408.6)
MP2 <sup>22</sup>	-1456.2	937.1	-219.1 (-1180.0)

In this work we adopt the RCCSD(T)-F12a method<sup>25</sup>, implemented in the MOLPRO package<sup>26</sup>, using the VDZ-F12 basis set<sup>27</sup>. Test calculations with larger basis set were done on the stationary points, obtaining essentially the same results. To check the adequacy of the RCCSD(T) method the T1 diagnostic<sup>28</sup> for a large variety of geometries being always smaller than 0.03, the larger value obtained at the saddle point, showing that multireference methods are not needed. This method is expected to be more accurate than all the previous ones, because the F12 method describes better the electronic correlation. All the geometries were optimized using the same RCCSD(T)-F12a method, and the re-

sults are shown in Table 1. We find a barrier of 19.5 and 27.1 meV, with or without ZPE, which we consider to be more precise than all previous values.

In all previous works<sup>21–24</sup> the reaction rate constants were calculated using the TST method with tunnelling based on the normal modes calculated at the saddle point. In order to go beyond TST methods, dynamical calculations have to be done, and in this work we shall use a QCT approach. In order to describe collisions at low temperature, a high correlated method as RCCSD(T)-F12 is required to have the proper accuracy of the PES. *Ab initio* molecular dynamics calculations are impractical because of the long computing time of a single point, and the high number of points on each individual trajectory at low collision energies. Thus an analytic fit is required to study the collision dynamics in these conditions, as described below.

### Analytic fit of the PES

The fit of the PES of systems for more than 4 atoms is a challenging problem, specially when devoted to reactive collisions. The method of Bowman *et al.*<sup>29</sup>, based on the direct fit with a many body term using permutationally invariant polynomials of the internuclear distances, has been applied to systems up to 10 atoms. **For example, this method has been succesfully used to study  $S_N2$  reactions<sup>30</sup> and water clusters<sup>31</sup>.** However, this method is not applicable to low temperatures because of the difficulty of describing long range interactions properly. Instead, here we use a variation of an alternative recently used to describe the proton transfer in  $H_4$  and  $H_5$ <sup>32–34</sup> considering properly the long range interactions.

In this approach, the electronic Hamiltonian matrix is separated in two terms as

$$H \quad H^{diab} \quad H^{MB} \quad (1)$$

where  $H^{diab}$  is an electronic diabatic matrix, in which each diagonal matrix element describes a rearrangement channel. Thus, reactants and products are properly described by these terms and also the long range interactions. In the case of  $H_4$  and  $H_5$  these terms were described by a triatomics-in-molecules method (TRIM)<sup>32,34</sup>, which is an extension of the diatomics-in-molecule (DIM)<sup>35,36</sup>. This allows to describe not only di- and triatomic products of physical relevance in those cases, but also a rather good description of the intermolecular interactions among them, including long range interactions. This method, however, is difficult to be extended to large polyatomic systems, as the one treated in this work. For this reason we shall use here a reactive force field (RFF)<sup>37</sup> approach, described below.

The  $H^{MB}$  term in Eq. (1) is a many-body term matrix added to get the desired accuracy. For describing the ground electronic state, a diagonal matrix with all elements being equal. This matrix element is expanded in terms of permutationally invariant polynomials<sup>38,39</sup>, as in the method of Bowman *et al.*<sup>29</sup>. In this case, the RFF does not have all permutation symmetry, but only the physically allowed by energy, *i.e.*, the permutation of the two equivalent hydrogen atoms of  $\text{H}_2\text{CO}$  reagent. As a consequence the MB term only consider this permutation symmetry. This term

must vanish at long distance in any rearrangement channel<sup>38</sup>.

## Reactive force field

Here we use the Empirical Valence Bond method<sup>40</sup>, which considers each rearrangement channel as a diabatic state that can be represented by an element of a matrix. The off-diagonal terms,  $V_{eff}$ , is an effective coupling term among the rearrangement channels, in such a way that the lowest eigenvalue of the matrix becomes continuous and describes the global potential for the ground electronic state. There are three rearrangement channels in this reaction, one for OH and H<sub>2</sub>CO reagents, and two for HCO + H<sub>2</sub>O products, leading to a 3 × 3 matrix representation of the RFF, represented as

$$H^{diab} = \begin{pmatrix} H_{11} & V_{eff} & V_{eff} \\ V_{eff} & H_{22} & 0 \\ V_{eff} & 0 & H_{33} \end{pmatrix} \quad (2)$$

where  $H_{11} = \frac{V^{OH}}{V^{H_aCO}} \frac{V^{H_2CO}}{V^{H_2O}}$ ,  $H_{22} = \frac{V^{H_aCO}}{V^{H_2CO}} \frac{V^{H_2O}}{V^{H_2CO}}$ , and  $H_{33}$  is equivalent to  $H_{22}$  but replacing hydrogen  $H_a$  by  $H_b$ . The zero of energy is set at the minimum of the reactants at long distances and  $-1.30$  eV corresponds the exothermicity of the reaction. Below we describe each of the terms separately.

a. PES of the fragments

The potential of isolated formaldehyde and water are described by a force field (FF) of the form

$$\begin{array}{ccccccc}
V^A & D_e & 1 & e & b & b_e & 2 \\
& b & & & & & \\
& & k & 0 & & k_{bb} & b \\
& & & & b & b & b_0 \\
& & & & & & b_0 \\
& & k & 0 & & 0 & \\
& & & & & & \\
& & k & b & b & b_0 & 0 \\
& b & & & & & 
\end{array} \quad (3)$$

with  $b$  corresponding to the internuclear distances of the bonds of the molecule, and  $\gamma$  are the angles between the bonds.  $\gamma_{\text{im}}$  are the improper dihedral angles of formaldehyde, absent in the case of water molecule, and the subindex 0 refers to the equilibrium value of each coordinate. The parameters are optimized to reproduce the *ab initio* points calculated along several classical trajectories in the harmonic potential calculated from the *ab initio* normal modes. For those coordinates leading to dissociation, further points were added to better adjust this process. The summary of number of points, errors of the  $\text{H}_2\text{CO}$  and  $\text{H}_2\text{O}$  fragments are listed in Table 2.

The PES for HCO presents several minima, and can not be properly described by such simple FF functional form. Instead, the HCO potential is represented by a many body expansion form fitting the parameters to reproduce the calculated *ab initio* points with the gfit3C program<sup>41</sup>. A summary of the fit is in Table 2.

Finally, the OH potential energy curve have been fitted to the

**Table 2** Errors (number of points in the energy interval considered) of the H<sub>2</sub>CO, H<sub>2</sub>O, HCO and OH fragments obtained in the fit.

Fragment	Error (meV)	
	$E - 1$ eV	$E - 2$ eV
H <sub>2</sub> CO	84.4 (3158)	111 (3781)
OH	4.42 $\cdot 10^{-3}$ (44)	6.33 $\cdot 10^{-3}$ (67)
HCO	93.0 (1322)	125 (2695)
H <sub>2</sub> O	63.8 (949)	393 (3029)

*ab initio* points following the method of Aguado and Paniagua<sup>42</sup>.

**b. Intermolecular PES**

The  $V^{OH-H_2CO}$  and  $V^{HCO-H_2O}$  interactions between fragments, defined below Eq. 2, are described by two terms: a long range term,  $V_{lr}$ , and a short range,  $V_{sr}$ , on each arrangement. The transition between long and short range potentials in the entrance channel is done with a smooth switching function based on a hyperbolic tangent function.

The long range term,  $V_{lr}$ , has been introduced for the leading dipole-dipole interaction between OH and H<sub>2</sub>CO systems, and neglected for the two HCO + H<sub>2</sub>O products, because the reaction is exothermic and these terms are not expected to play an important role. The dipole of OH ( $\mathbf{d}_{OH}$ ) and H<sub>2</sub>CO ( $\mathbf{d}_{H_2CO}$ ) reagents with respect to their corresponding center-of-mass have been calculated at their equilibrium geometries, and is considered to be constant because the dipole of each fragment does not vary significantly with the vibrations. The long range potential is then given by the usual dipole-dipole interaction term<sup>43</sup>

$$V_{lr} = \frac{R^2 \mathbf{d}_{OH} \cdot \mathbf{d}_{H_2CO} - 3 \mathbf{d}_{OH} \cdot \mathbf{R} \mathbf{d}_{H_2CO} \cdot \mathbf{R}}{4 R^5} \quad (4)$$

where  $\mathbf{R}$  is the vector between the two centers of mass.

The short range term,  $V_{sr}$ , is represented by a sum of pair interactions between all atoms belonging to different fragments. Either Morse potentials, Lennard-Jones like or fully repulsive functions have been used to obtain the better fit to these interactions. The choice of the function is done by looking at the behavior of the *ab initio* calculations along several approaching geometries, and the parameters are fitted to reproduce in average the interaction on several of them.

**c. Coupling between rearrangements**

The  $V_{eff}$  terms in Eq. 2 introduce a coupling between the different rearrangement channels. These terms are carefully designed to reproduce the height and position of the saddle point, which should appear in the region where the "diabatic states" cross. In the present approach, we shall neglect the coupling between the two equivalent product channels 2 and 3. The couplings between the reactant channel 1 and the two product channels, 2 and 3, are equivalent, and we shall consider an unique effective coupling function  $V_{eff}$ , with the form

$$V_{eff} = C e^{-E^{2q}} g(r_{OH}) g(r_{CH}) g(r_{CH}) g(r_{OH}) \quad (5)$$

with  $C$  being the coupling strength,  $E^2$  the square of the difference in energy of the reactant and the closest product diabatic

state, 2 or 3, and  $q$  are the parameters introduced to modulate the intensity as a function of the energy difference. Note, that  $q$  must be larger than 1 to avoid discontinuity in the derivatives when  $\Delta E = 0$ . Finally,  $g(x)$  is a damping function to localize the couplings in the region of the saddle point, where  $r_{OH}$  and  $r_{CH}$  are the distances of the breaking/forming bond.

**Many-body term**

The matrix element  $H^{MB}$  used to fit the *ab initio* energies is expanded as polynomials in the Rydberg variables expressed in terms of all the internuclear distances ( $R = 1 - 6$ )<sup>39</sup>. To make the potential invariant with respect to the interchange of indistinguishable nuclei, the polynomials are symmetrized using the Young operator corresponding to the totally symmetric irreducible representation of the  $S_n$  permutation group of  $n$  objects. The  $3 \times 3$   $H^{diab}$  matrix takes into account only the permutation of the two equivalent hydrogen atoms of H<sub>2</sub>CO reagent. Hence the unnormalized Young operator,  $\frac{1}{2}(1 + P_{12})$  corresponds to the  $S_2$  group,

$$w^2 = \frac{1}{2} (1 + P_{12})$$

where  $P_{12}$  is the permutation operator that interchange the two equivalent hydrogen of H<sub>2</sub>CO (named a and b). The application of  $\frac{1}{2}(1 + P_{12})$  to the product of the Rydberg variables  $\prod R_i e^{-R_i}$ , gives the symmetry adapted functions (SAF) permutationally invariant with respect to the interchange of both equivalent hydrogen nuclei,

$$r^{SAF} = \frac{1}{2} (r^2 + r_i^2)$$

where  $i$  are the power of the variable of the polynomial, and  $r = r_i$ . The order of this polynomial is  $i$  and will be used to select the terms included in the fit. In addition, the non linear exponents of the Rydberg variables must be optimized taking into account the permutation symmetry, that impose  $i_1 = i_2$  for  $i_3 = i_6$ .

The functional form for the six-body potential in terms of this SAF polynomials takes the form

$$H^{MB} = \sum_r \sum_i c_r r^{SAF}$$

where the sum run over  $r$ . In this sum we exclude the terms that correspond to two, three, four and five body potentials, that are included in the  $H^{diab}$ . This impose constraints on the  $r = i$  permitted values. With this restriction the number of terms of the polynomial are: 680 for the degree five and 5932 for the degree six. In order to use an intermediate number of parameters, we have imposed the restriction  $i = 0$  or 1, that gives 2596 terms for the six order polynomial in the present case.

**Fit procedure and results**

In the fit procedure of the MB term it is necessary to reproduce the transition state region very accurately. For this reason, the intrinsic reaction coordinate (IRC) between the two deepest wells of the reactant and products channels have been calculated with the **RCCSD(T)-F12a** method (shown in Fig. 1). Also, the nor-

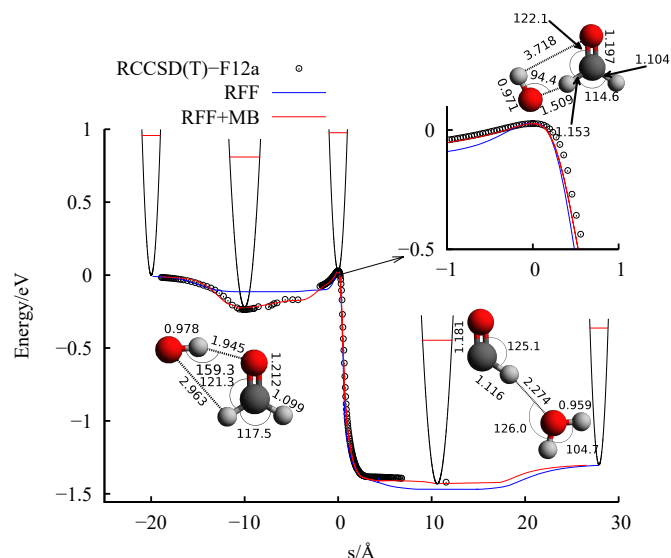


**Fig. 1** *Ab initio* IRC, compared with the RFF and the RFF+MB complete fit. The insets indicate the geometry of the  $\text{H}_2\text{CO} \cdots \text{OH}$  and  $\text{HCO} \cdots \text{OH}_2$  complexes and of the saddle point (with distances in Å). The points from the minima to the corresponding reactants and products asymptotes, respectively, are calculated with a steepest descent method from the asymptotes to the minima. The variable  $s$  is evaluated from the geometries as usually done for the IRC.

mal modes along the IRC were calculated, and *ab initio* points were calculated as a function of each normal coordinate. All these points were included in the fit with a larger weight ( $\sim 500$  below 5 eV) to get a good accuracy at the transition state region.

In total about 150000 *ab initio* points have been calculated, of which approximately 100000 have an energy lower than 10 eV (with respect to the asymptotic  $\text{OH} + \text{H}_2\text{CO}$  energy at the equilibrium geometry, here after consider as zero of energy). These points are introduced in the fitting procedure of the many body-term,  $H^{MB}$ , with a weight which decreases as energy increase over 5 eV over the reactant energy. The points have been calculated in different forms. First, regular grids in the reactant and products channels were calculated to characterize them at the equilibrium geometry of the fragments. Second, selected points chosen along classical trajectories run in different versions of the fit. Since the fit typically introduces oscillations in the potential, classical trajectories at 1eV (plus the ZPE) were used to locate the spurious minima. *Ab initio* calculations were performed at these points and introduced in a new fit. This procedure was repeated iteratively until no spurious minima were found running more the  $10^4$  trajectories. Also, artificial barriers were located by running trajectories at low kinetic energies (1 meV plus ZPE), determining the geometry of the rebound configuration, to add more points. Finally, random points were added at different geometries.

In the fitting procedure we optimize the 2596 linear  $c_r$  and 11 non-linear parameters. Because the non-linear optimization is computationally expensive, we have done the optimization of the non-linear parameters with the polynomial of order five. We have found that the fitted six-body term of the potential must correct both the short- and intermediate- regions of the potential.

In order to warranty this, the non-linear parameter were set to be larger than 0.85. With this requirement the MB term of the potential goes to zero as any internuclear distance goes larger than 10 a.u., ensuring the long range behavior of the potential given by  $V_{lr}$ .

**Table 3** Analysis of the errors of the RFF and RFF+MB fits, in meV. The number of points in each energy interval considered is also shown.

Points	Energy	Error RFF	Error RFF+MB
228	IRC	75.8	29.3
101	IRC( 1 s 1)	55.3	11.8
240	NM (E 1 0 eV)	68.2	11.5
27728	E 0 0 eV	111.2	70.5
76486	E 1 0 eV	146.7	77.5
95734	E 5 0 eV	1218	126

The root-mean-square errors are listed in Table 3. For energies below 1eV (well above the saddle point) the error of the RFF+MB PES is 77.5 meV, about a half of the error of the RFF one. This energy is slightly higher than the energy of the reactant plus the ZPE as can be seen in Fig. 1, covering essentially all the energy range of interest in this work. This error is much lower along the IRC, as shown in this Fig. 1: the error of the RFF+MF fit is of 29.3 meV, and around the saddle point of only 11.8 meV, significantly lower than that of the RFF fit alone. The height of the saddle point of the RFF+MB PES is 26.3 meV while the *ab initio* value is 27.1 meV. This small error (less than 1 meV) was possible because the RFF saddle point is 27.4 meV by design. Also, at each intermediate fit made, the IRC was calculated and more *ab initio* points were added along the one-dimension cuts of the normal modes.

The dependence of the fits on the normal coordinates at the saddle point of the RFF+MB fit is shown in Fig. 2. It is seen that the RFF+MB fit describe very well the *ab initio* points up to a rather high energy, always improving the description of the RFF PES. The harmonic frequencies (real and imaginary) obtained at the saddle points of the RCCSD(T)-F12a and RFF+MF potentials are also shown for each of the normal mode. All this analysis demonstrate that the RFF+MB fit describe rather accurately the TS region, with an error lower that the overall error shown in Table 3. It can also be seen that some of the modes are very anharmonic, specially those with frequencies 1265.5, 1342.6, 1450.6, 3029.3 3762.5 and 701.7i  $\text{cm}^{-1}$ . The out-of-plane modes (with frequencies 169.9, 321.1 and 1130.3  $\text{cm}^{-1}$ ) are symmetric but very flat at the well, also indicating a behavior far from harmonic as  $q_i^2$ . This indicate that the harmonic ZPE is not a good approximation, and anharmonic terms are expected to be rather important.

The long range region is of particular interest since it determines the dynamics at low energies, as will be discussed below. In Fig. 3 we compare the *ab initio* and the RFF potential for the long range part of the potential, for  $\text{H}_2\text{CO}$  in its equilibrium configuration and two different orientations of OH (in the equilibrium distance) around the  $\text{H}_2\text{CO}$ , either with the H ( $=0$  in top panels)



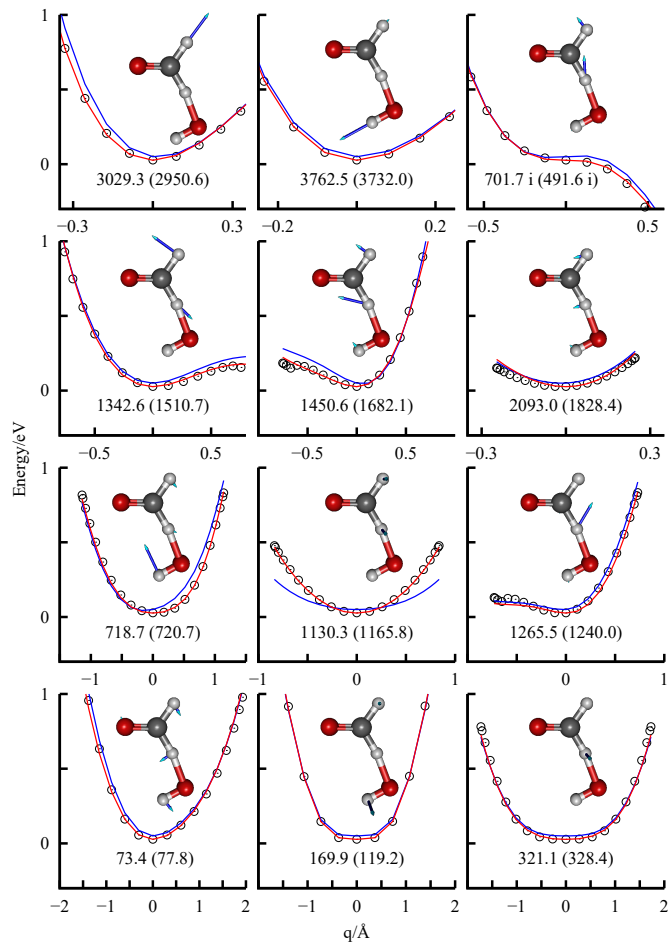


**Fig. 2** *Ab initio* points versus RFF (in blue) and RFF+MB (in red) fits along the monodimensional normal coordinates,  $q_i$ , obtained at the saddle point of the RFF+MB PES. In the inset each normal mode is shown. Also The harmonic frequency of the RFF+MB (*ab initio*) normal modes are indicated.

or O (in bottom panels) atom pointing towards the  $\text{H}_2\text{CO}$  center-of-mass. The complete RFF+MB fit is identical to the RFF one in this region. The agreement between the *ab initio* and the RFF PES is excellent. It also shows that the interaction is about 0.5 meV at  $R = 50$  a.u.

A detail of the PES is shown in Fig. 4 to analyze the quality of the fit, at the same orientation of the Fig. 3. The RFF (in the middle panels) is slightly too isotropic, being essentially attractive/repulsive for H/O pointing towards  $\text{H}_2\text{CO}$ . The addition of the MB term improves the description, allowing a better description of the anisotropy, in particular in the depth of the potential wells and extension in most of the cases. Some artifacts still remain at short distances. For example, in the bottom right panel, there is a repulsive ring, relatively low ( $\sim 10$  meV) but absent in the *ab initio* case (left bottom panel). This artificial ring is surrounded by an attractive ring, in agreement with the *ab initio* results. We finally conclude, that the present RFF+MB PES has a high accuracy at the saddle point and the long range region.

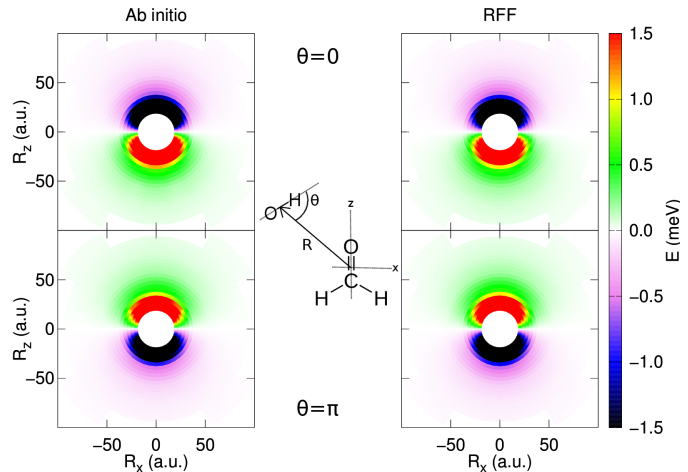


**Fig. 3** Contour plots of the PES calculated with the RCCSD(T)-F12a *ab initio* points with the VDZ-F12 basis set (left panels) and the RFF (right panels). The  $\text{H}_2\text{CO}$  in its equilibrium geometry in the  $xz$  plane, with its center of mass at the origin and the CO bond along the  $z$  axis, as shown in the inset.  $R$  is the vector joining  $\text{H}_2\text{CO}$  and OH center-of-mass, with components  $R_x$  and  $R_z$ . The white circles in the figure indicate the region expanded in Fig. 4.

## Quasi-classical trajectory calculations

### Reactive cross section

Quasi-classical trajectory (QCT) calculations on the  $\text{H}_2\text{CO} + \text{OH}$  reaction have been done on the RFF+MB PES in a recent publication<sup>19</sup>. In this work we shall analyze in more detail those results to get further physical insight of the reaction mechanism. The calculations were done with an extension of the miQCT code<sup>44,45</sup> applied to N atoms, and the details of the method and parameters used were described before<sup>19</sup> and are omitted here. For  $\text{H}_2\text{CO}$  and OH in their ground vibrational and rotational states, the reactive cross section at fixed collision energies were calculated as<sup>46</sup>

$$\sigma_j(E) = b_{\max}^2 P_r(E) \quad \text{with} \quad P_r(E) = \frac{N_r}{N_{\text{tot}}} \quad (6)$$

where  $N_t$  is the maximum number of trajectories with initial impact parameter lower than  $b_{\max}$ , the maximum impact parameter for which reaction takes place, and  $N_r$  is the number of trajectories leading to products. The initial conditions were sampled using a Monte Carlo method<sup>19</sup>, and the initial impact parameter is randomly set in the interval  $[0, B]$ , with  $B$  being set according to a capture model<sup>47</sup> as

$$B = \sqrt{\frac{A}{2E}} \quad (7)$$

for a dipole-dipole interaction, Eq. (4), varying as  $A/R^3$  for long distances  $R$  between the center-of mass of the two reactants (with  $A = 4d_{\text{OH}}d_{\text{H}_2\text{CO}}$  corresponding to the optimal orientation between the permanent dipoles of the two reactants). About  $10^5$  trajectories have been calculated for each collision energy between 0.1 meV and 250 meV, and the cross section obtained is shown in Fig. 5.

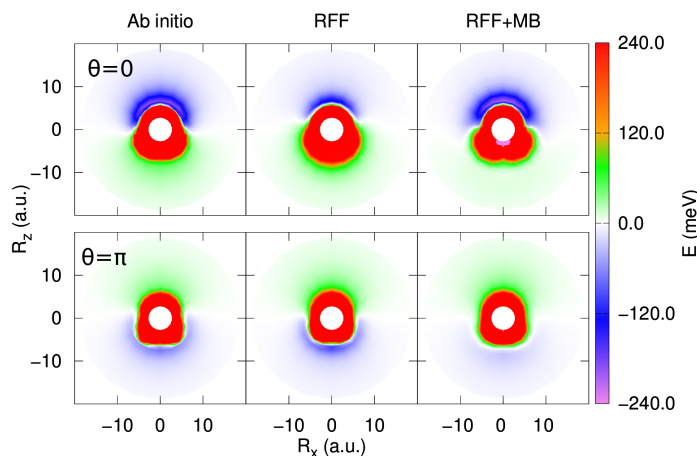


**Fig. 4** Contour plots of the PES calculated with the *ab initio* points (left panels), the RFF (middle panels) and RFF+MB fit (right panels), for comparison. The geometries are the same of Fig. 3, but for shorter distances.

The reactive cross section increases by nearly 3 orders of magnitude when collision energy reduces from 1000 to 0.1 meV. The energy of the transition state, with or without ZPE, does not affect at all to this behavior, and this happens for the two PESs. However, the RFF results are nearly 10 times larger than those obtained with the full RFF+MB PES. In order to explain these surprising results we shall use Eq (6) and discuss separately the effect of the impact parameter,  $b$ , and the reaction probability,  $P_r$ , in the cross section.

### Capture and impact parameter

The impact parameter,  $b$ , shown in Fig. 6, increases continuously with decreasing collision energy, and closely mimic the results obtained with the capture model. As collision energy decreases, the potential is able to deviate the trajectories from longer distances to make the reactants approach each other. This increase of the impact parameter is clearly the responsible for the increase of the cross section as energy decreases.

The capture process is illustrated in Fig. 7 for two typical trajectories, with large and small initial impact parameter. In trajectories with small impact parameter, the two reactants approach each other, rebound a couple of times and then the reactants or products fly apart. However, trajectories with large initial impact parameter, and hence large end-over-end angular momentum, follow a long circular orbit, until a complex between reactants is formed. Within this complex, the two reactants continue rotating while they collide many times.

During this long approaching orbits, the relative orientation of the reactants also changes, as it is shown in Fig. 8. The  $\mathbf{d}_{OH}$  and  $\mathbf{d}_{H_2CO}$  electric dipoles are along the OH and CO bonds, respectively. For the long trajectory of Fig. 7, the angles formed by the electric dipoles and the vector  $\mathbf{R}$  vary around 0 for  $\mathbf{d}_{OH}$

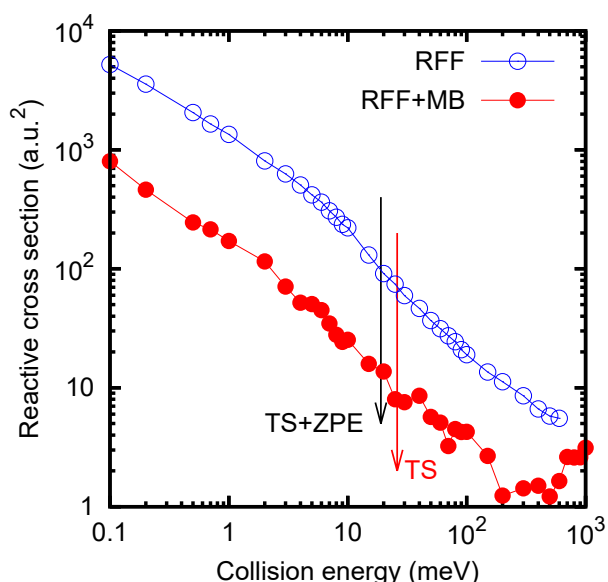


**Fig. 5** Integral reactive cross section for the  $H_2CO + OH \rightarrow HCO + H_2O$  reaction with the two reactants initially in their ground vibrational and rotational state.

and  $\mathbf{d}_{H_2CO}$ , respectively. These geometries correspond to the situation in which the interaction gets more attractive, and since this interaction grows as  $R$  decreases, the amplitude of the oscillations decreases. Similarly, the angle between the two dipoles also varies around  $\pi$ , orientation at which the dipole-dipole interaction is more attractive.

Because of this reorientation along the approaching trajectories, the two reactants start to rotate, and this rotational motion is accelerated as the reactants get closer. The rotational energy of the two fragments may get significant values as compared to the very low initial collision energies simply because the available kinetic energy is of the order of the well depth.

Once a molecular system starts to rotate, it is difficult that the rotation stops completely by colliding with the other partner. The rotational energy is larger than the collision energy required to escape back again, since a single rotational quantum of the OH ( $\approx 2.5$  meV) is much larger than the energy required to fly apart. Therefore the system can not separate again because it does not have available energy in the translation degrees of freedom and the system becomes trapped in the well for a long time. In Fig. 9 the evolution of the trajectories with time shows that the complex time for large initial parameter is rather long, of the order to 10-20 ps. This time is however about one order of magnitude shorter than the time the reactants require to approach each other, of the order of several hundreds of ps.

### Collision complex lifetime and reaction probability

The trajectories trapped forming the complex, sample a large region of the configuration space (see Figs. 7 and 9) and may be considered to become ergodic. According to the RRKM statistical theory<sup>48,49</sup>, the lifetime of the collision complex depends on the



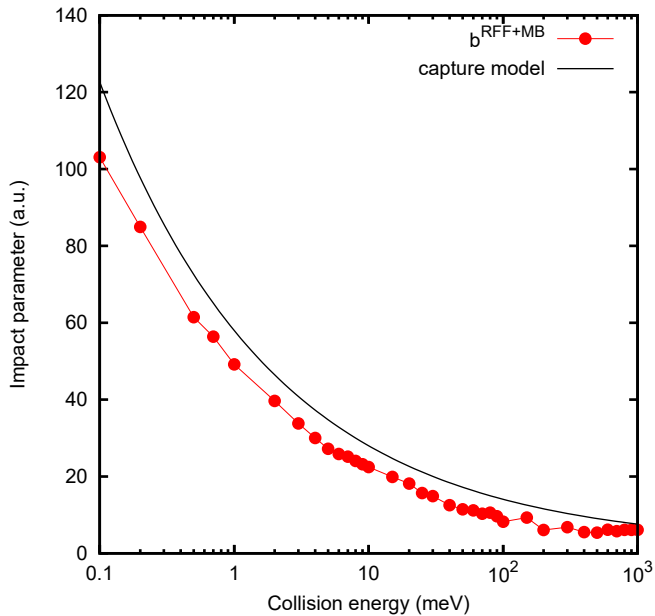


**Fig. 6** Maximum impact parameter for the  $\text{H}_2\text{CO} + \text{OH} \rightarrow \text{HCO} + \text{H}_2\text{O}$  reaction with the two reactants initially in their ground vibrational and rotational state.

number of open channels,  $N_o$ , as

$$2 \hbar \frac{E}{N_o E} \quad (8)$$

where  $E$  is the density of states of the complex at energy  $E$ . This situation is analogous to the situation of ultracold collisions<sup>50</sup>, where just one or very few open channels are available. Thus the collision complex have very long lifetimes, and virtually explore all the states contributing to  $E$ .

In Fig. 10 the average lifetimes for the ensemble of trajectories reacting or not are shown separately. The collision complex lifetime of non-reactive trajectories shows a sudden increase when the number of OH rotational levels reduces to just 1, what also reduces significantly the accesible levels of  $\text{H}_2\text{CO}$  by angular momentum conservation.

On the contrary, for reacting trajectories, the collision complex lifetime is rather smooth and do not depend on the rotational levels of the OH and  $\text{H}_2\text{CO}$  reactants, but instead it may be considered that it depends on the products density of levels: the number of open products channels is considerably large and constant in this energy interval because the reaction is highly exothermic.

The structure of the collision complex lifetime for reacting trajectories closely mimic the reaction probability shown in the top panel of Fig. 10. This may indicate that there is a connection between collision complex lifetime of reacting trajectories and reaction probability. The question that remains to answer is why the reaction probability is non zero at energies below the top of the barrier.

Considering the ZPE of reactants, the system has enough total energy to overcome this barrier. If the reactants ZPE remains in the coordinates orthogonal to the reaction coordinate, the reaction could not take place, since there would not be enough

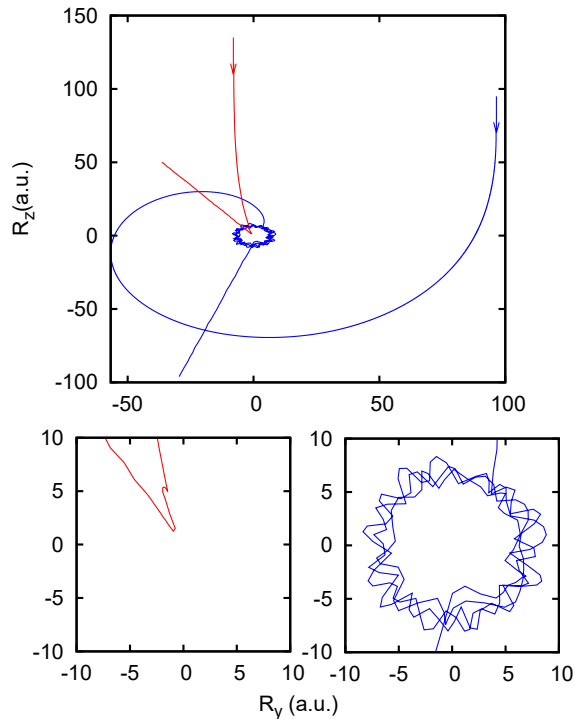


**Fig. 7** Typical trajectories at collision energy of 0.1 meV with large (blue) and small (red) initial impact parameter, as a function of  $R_x$  and  $R_y$  in the system of coordinates described in Fig. 3. The insets show each individual trajectory at shorter  $R$  values.

energy in the reaction coordinate. Clearly, this is not the case, and there must be couplings between the reaction coordinate to the remaining degrees of freedom, producing an energy transfer which explains the non zero reaction probability even at 0.1 meV of collision energy.

Such situation is typical in non-IRC trajectories<sup>51</sup>, since they explore large regions of the configuration space, far from the minimum energy path determined by the IRC where the anharmonicity is larger. The trajectory shown in Figs. 7 and 9 clearly show a roaming behavior<sup>52,53</sup> in which the fragments explore geometries very far from the IRC where the anharmonicity of the PES is higher producing energy transfer among all the degrees of freedom. Moreover, the ZPE at the transition state is calculated in the harmonic approximation, and it is expected to be considerably reduced when anharmonic effects, as those discussed in Fig. 2, are considered.

The reaction probability obtained for the RFF PES is much larger than that for the RFF+MB PES, and this is the reason of the large difference observed in the corresponding cross sections in Fig. 5. This difference is clearly not due to the height of the saddle point, since the higher TS is for the RFF, as can be seen in Fig. 1. Since for the two PES's the trajectories are trapped by the long range term of the potential, the difference should be associated to the access from the well in the entrance channel to the saddle point for the reaction. The RFF is by far more simple, and does not describe properly the anisotropic character of the PES, giving an easier access to the TS region.

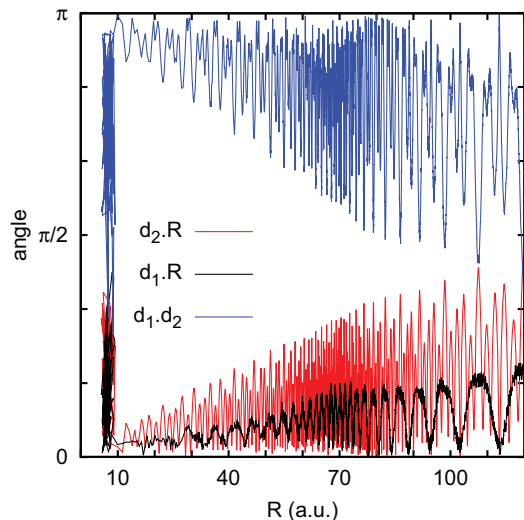


**Fig. 8** Variation of the angles between  $\mathbf{R}$  and  $\mathbf{d}_1$  (black),  $\mathbf{R}$  and  $\mathbf{d}_2$  (red) and  $\mathbf{d}_1$  and  $\mathbf{d}_2$  (blue) for the trajectory of large impact parameter of Fig. 7

### Quantum effects

As reaction probability is related to the lifetime of the collision complex, and this depends on the number of open channels, it is expected that quantum effects are important in this energy regime. Traditional quantum methods are not applicable for so many degrees of freedom and so low energies. On the other hand, a traditional way to correct QCT calculations is to neglect those trajectories which do not fulfill the ZPE requirement. However, in doing so most of inelastic trajectories will be discarded, while reactive trajectories not, and hence the reaction probability and reactive cross section would increase too much. One alternative is to use semiclassical methods, such as the ring polymer molecular dynamics approach<sup>54–57</sup> or centroid dynamics<sup>58,59</sup>, both based on the path integral method. It is however a challenge to use these methods for such low temperatures of interest here.

Nevertheless we shall discuss about the qualitative behavior of QCT based methods to describe the reaction dynamics in this case. It is noticeable, that rotational excitation plays an important role in the dynamics in the entrance channel, through the dipole-dipole long range interaction that make the system form a long lived collision complex. The  $\text{OH} + \text{F} \rightarrow \text{HF} + \text{O}$  reaction has a similar dynamics and energy profile and, being a triatomic system, exact quantum wave packet and QCT calculations have been performed<sup>60–62</sup>. It was found that in this exothermic reaction, the quantum reactive cross section increases significantly at low energies<sup>61,62</sup>. This increase was due to the formation of long lived resonance in the entrance channel in which OH was rotationally excited as in  $\text{H}_2\text{CO} + \text{OH}$ . The reaction probabilities calculated with a QCT method in this triatomic system showed peaks, which were associated to quasi-periodic orbits, and these peaks were in semiquantitative agreement with the corresponding quantum calculations. These resonance structures persist in  $\text{OH} + \text{F}$  reaction for high partial waves, and manifest in an increase of the cross section at low collision energies, in both quantum wave packet and QCT calculations<sup>60–62</sup>. However, the QCT results yielded a lower increase in the cross section, what was attributed to a lack

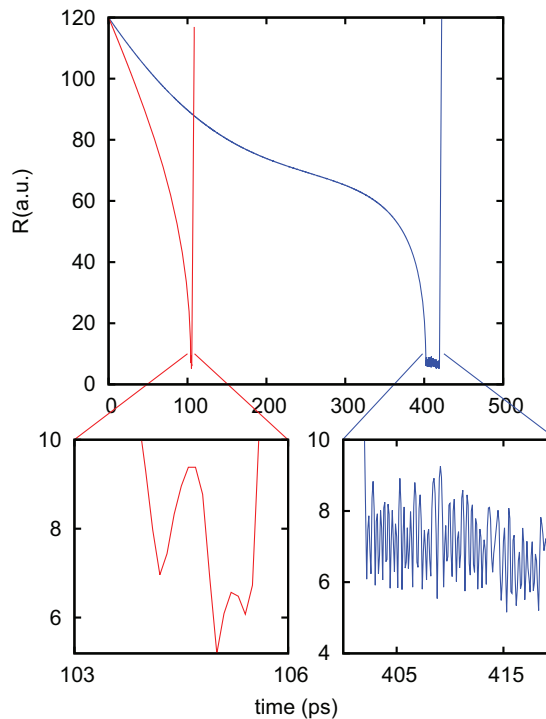


**Fig. 9** Trajectories of Fig. 7 showing the evolution of  $R$  with time. The insets show the evolution of the collision complex.

of accuracy in describing resonance lifetime.

Analogously, in the  $\text{H}_2\text{CO} + \text{OH}$  results we expect also an underestimation of the cross section at low energies based on the previous example. Work in this direction is in progress.

### Rate constants and comparison with experiment

The initial state selected rate constant (corresponding to OH and  $\text{H}_2\text{CO}$  in their ground vibrational and rotational state) is obtained by integrating the cross section over a Boltzmann distribution. The spin-orbit splitting of the electronic states of  $\text{OH}(^2\Pi)$  states (into the  $F_1(^2\Pi_{1/2})$  and  $F_2(^2\Pi_{3/2})$ , with an energy separation of 200.279 K) should be taken into account. Assuming that two states correlating to the ground  $F_2(^2\Pi_{3/2})$  react, and the other two do not, the rate constant has to be multiplied by the factor  $q_e(T) = 1/(1 + \exp(-200.3/T))$ , arising from the electronic partition function, where  $k_B$  is the Boltzmann constant. The final state selected rate,  $K_{j=0}(T)$ , is shown in Fig. 11, and it decreases with increasing temperature in the range studied. This behavior is expected after the analysis of the cross section, in Fig. 5, but, for  $T > 50\text{K}$ , the decrease is also due to the  $q_e(T)$  factor.

In order to compare with the experiment, the thermal rate constant is also calculated running more the 1 million of trajectories for each temperature in the macracanonical ensemble<sup>19</sup> as,

$$K(T) = q_e(T) \sqrt{\frac{8k_B T}{\pi \mu}} \pi b_{\max}^2(T) P_r(T), \quad (9)$$

where  $\mu = m_{\text{OH}} m_{\text{H}_2\text{CO}} / (m_{\text{OH}} + m_{\text{H}_2\text{CO}})$  is a reduced mass.  $b_{\max}(T)$  and  $P_r(T)$  are the maximum impact parameter and reaction prob-

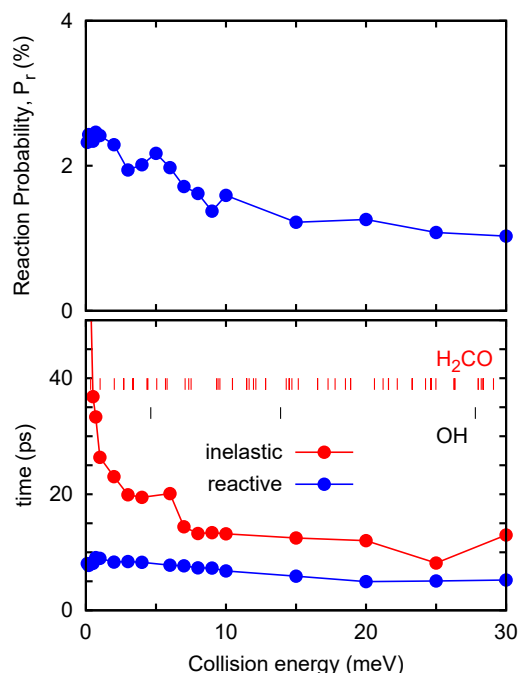


**Fig. 10** Top panel: reaction probability associated to the cross section shown in Fig. 5. Bottom panel: Average complex lifetimes for trajectories reacting (blue) and non-reacting (red). The rotational energies of OH and H<sub>2</sub>CO are also shown.

abilities defined above, but now for each temperature. The results obtained are shown in Fig. 11 and compared with the recent experimental rate constants of Ocaña *et al.*<sup>19</sup>

The state-selected  $K_{j=0}(T)$  rate constant is always larger than the thermal rate constant  $K(T)$ . The reason is that the capture mechanism described here is disrupted for excited rotational states of OH. First, the relatively high rotational energy of OH( $j=1$ ) ( $\sim 5$  meV) makes more difficult to orient this fragment making less efficient the capture. Second, the higher rotational energy open more channels, specially significant in the reactant rearrangement channels, what reduces the lifetime of the collision complex. All this make less efficient the reaction as the rotational excitation grows higher, and this effect is now under study.

The calculated thermal rate constant is approximately a factor of 2 lower than the two sets of experimental data, but the overall decrease is semiquantitatively correct, demonstrating that this reaction does not show a threshold for temperatures above 10K. The lack of complete agreement between the theoretical and experimental results can be attributed at least to two reasons. First, the PES, due to the difficulty of getting a potential with an accuracy better than 10K. The zero point energy of the reagents is  $\sim 1$  eV, and the exothermicity is 1.3 eV. This would imply a relative error below 0.1% for a system with 12 internal degrees of freedom, which is now a days a challenge. Second, quantum effects are expected to increase the lifetimes of the collision complexes, as discussed above. This would produce an increase of the reaction rate. Work in these two directions is now in progress.

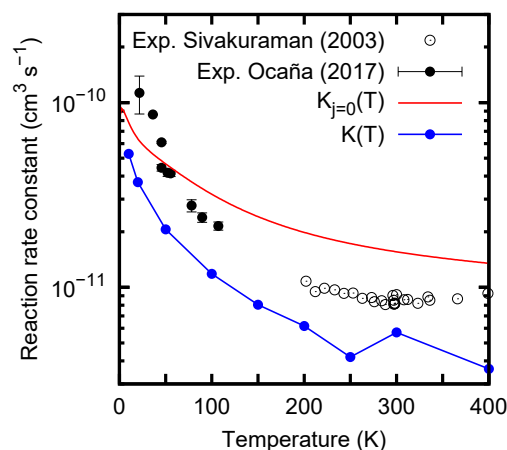


**Fig. 11** Calculated reactive rate constants (thermal  $K(T)$  and state-selected  $K_{j=0}(T)$  as described in the text) versus the experimental results of Ocaña *et al.*<sup>19</sup> and Sivakuraman *et al.*<sup>63</sup>.

## Conclusions

In this work a method has been developed to represent the multidimensional potential energy surface of reactions, like OH + H<sub>2</sub>CO, with analytical functions, describing accurately the long range interaction and the saddle point. This kind of potentials are required to describe the collisions at the low temperatures of the interstellar medium (of  $\sim 10$  K) and it has been applied to the study OH + H<sub>2</sub>CO  $\rightarrow$  H<sub>2</sub>O + HCO reaction. The reactive rate constants have been calculated using a Quasi-classical trajectory method between 10 and 400 K, and the results are in good agreement with the experimental data.

This reaction presents a low barrier for the reaction, of 27.4 meV  $\sim 318$  K, but the measurements and calculations show that the reaction rate constant increases as the temperature decreases down to  $\sim 10$ -20 K. This fact was previously explained in the framework of transition state theory introducing tunnelling. In the present classical calculations, it is simply an energy transfer between the vibrational modes and the reaction coordinate, induced by the formation of a collision complex leading to long lived roaming trajectories.

Quantum effects are expected to play a role and should be analyzed. However, rotation plays a major role in the energy transfer mechanism and minimize the zero-point energy problem. This has been analyzed in a similar system like OH + F, for which quantum results have been calculated, indicating that the reactive cross section increases with decreasing collision energy in both quantum and classical results, with classical ones being in general lower.

This reaction mechanism may have an important effect in astrophysical models of dense molecular clouds at temperatures of 10K, where many gas phase reactions have been neglected because they show a reaction barrier. Many of these reactions have to be readdressed in order to determine if this mechanism is possible and may give a noticeable rate constant. For this purpose, the method developed in this work to represent analytically the potential energy surface of polyatomic systems is of great importance.

## Acknowledgements

We acknowledge the support of Ministerio de Economía e Innovación (Spain), for grants CSD2009-00038, AYA2016-75066-C2-1-P, RyC-2014-16277 and FIS2014-52172-C2 and from the European Research Council under the European Union's Seventh Framework Programme (FP/2007-2013) / ERC Grant Agreement n. 610256 (NANOCOSMOS). E. Jiménez acknowledges the Spanish Ministry of Economy and Competitiveness for supporting this work under the GASSOL project (CGL2013-43227-R). AC is indebted to the French National Programme "Physique et Chimie du Milieu Interstellaire" (PCMI) of CNRS/INSU with INC/INP co-funded by CEA and CNES. We also acknowledge the financial support of the European COST program, CM1401, "Our Astrochemical History". The calculations have been performed CSIC computing centers, which are acknowledged.

## References

- 1 M. Ohishi, *J. Phys. Conf. Ser.*, 2016, **728**, 052002.
- 2 E. Herbst and E. F. van Dishoeck, *Annu. Rev. Astro. Astrophys.*, 2009, **47**, 427.
- 3 L. E. Snyder, D. Buhl, B. Zuckerman and P. Palmer, *Phys. Rev. Lett.*, 1969, **22**, 679.
- 4 J. A. Ball, C. A. Gottlieb, A. E. Lilley and H. E. Radford, *AstroPhys. J.*, 1970, **162**, L203.
- 5 R. L. Hudson and M. H. Moore, *Icarus*, 1999, **140**, 451.
- 6 N. Watanabe, O. Mouri, A. Nagaoka, T. Chigai, A. Kouchi and V. Pirronello, *AstroPhys. J.*, 2007, **668**, 1001.
- 7 A. G. G. M. Tielens and W. Hagen, *Astron. Astrophys.*, 1982, **114**, 245.
- 8 N. Watanabe and A. Kouchi, *AstroPhys. J.*, 2002, **571**, L173.
- 9 K. M. Pontoppidan, E. F. van Dishoeck and E. Dartois, *Astron. Astrophys.*, 2004, **426**, 925.
- 10 G. W. Fuchs, H. M. Cuppen, S. Ioppolo, C. Romanzin, S. E. Bisschop, S. Andersson, E. F. van Dishoeck and H. Linnartz, *Astron. Astrophys.*, 2009, **505**, 629.
- 11 R. T. Garrod, I. H. Park, P. Caselli and E. Herbst, *Faraday Discuss.*, 2006, **133**, 51.
- 12 G. A. Cruz-Díaz, R. Martín-Doménech, G. M. Muñoz-Caro and Y.-J. Chen, *Astron. Astrophys.*, 2016, **592**, 68.
- 13 M. Bertin, C. Romanzin, M. Doronin, L. Philippe, P. Jeseck, N. Ligterink, H. Linnartz, X. Michaut and J.-H. Fillion, *AstroPhys. J. L.*, 2016, **817**, L12.
- 14 R. J. Shannon, M. A. Blitz, A. Goddard and D. E. Heard, *Nature Chem.*, 2013, **5**, 745.
- 15 J. C. Gómez-Martín, R. L. Caravan, M. A. Blitz, D. E. Heard and J. M. C. Plane, *J. Phys. Chem. A*, 2014, **118**, 2693.
- 16 M. Antiñolo, M. Agúndez, E. Jiménez, B. Ballesteros, A. Canosa, G. E. Dib, J. Albadalejo and J. Cernicharo, *AstroPhys. J.*, 2016, **823**, 25.
- 17 W. Siebrand, Z. Smedarchina, E. M.-N. ez and A. Fernández-Ramos, *Phys. Chem. Chem. Phys.*, 2016, **18**, 22712.
- 18 R. J. Shannon, J. C. G. Martín, R. L. Caravan, M. A. Blitz, J. M. C. Plane, D. E. Heard, M. Antiñolo, M. Agúndez, E. Jiménez, B. Ballesteros, A. Canosa, G. E. Dib, J. Albadalejo and J. Cernicharo, *Phys. Chem. Chem. Phys.*, 2017, **submitted**.
- 19 A. J. Ocaña, E. Jiménez, B. Ballesteros, A. Canosa, M. Antiñolo, J. Albadalejo, M. Agúndez, J. Cernicharo, A. Zanchet, P. del Mazo, O. Roncero and A. Aguado, *AstroPhys. J.*, 2017, **submitted**.
- 20 A. Zanchet, B. Bussery-Honvault, M. Jorfi and P. Honvault, *Phys. Chem. Chem. Phys.*, 2009, **11**, 6182.
- 21 J. R. Alvarez-Idaboy, N. Mora-Diez, R. J. Boyd and A. Vivier-Bunge, *J. Am. Chem. Soc.*, 2001, **123**, 2018.
- 22 B. D'Anna, V. Bakken, J. A. Beukes, C. L. N. nd K. Brudnik and J. T. Jodkowski, *Phys. Chem. Chem. Phys.*, 2003, **5**, 1790.
- 23 Y. Zhao, B. Wang, H. Li and L. Wang, *J. Mol. Struct.*, 2007, **818**, 155.
- 24 M. Akbar-Ali and J. R. Barker, *J. Phys. Chem. A*, 2015, **119**, 7578.
- 25 G. Knizia, T. B. Adler and H. J. Werner, *J. Chem. Phys.*, 2009, **130**, 054104.
- 26 MOLPRO is a package of ab initio programs designed by H. -J. Werner and P. J. Knowles and with contributions from , J. Almlöf and R. D. Amos and A. Berning and M. J. O. Deegan and F. Eckert and S. T. Elbert and C. Hampel and R. Lindh and W. Meyer and A. Nicklass and K. Peterson and R. Pitzer and A. J. Stone and P. R. Taylor and M. E. Mura and P. Pulay and M. Schütz and H. Stoll and T. Thorsteinsson and D. L. Cooper, version 2012.
- 27 K. A. Peterson, T. B. Adler and H. J. Werner, *J. Chem. Phys.*, 2008, **128**, 084102.
- 28 J. Lee and R. Taylor, *International Journal of Quantum Chemistry*, 1989, **36**, 199.
- 29 B. J. Braams and J. M. Bowman, *Int. Rev. Phys. Chem.*, 2009, **28**, 577.
- 30 Y. Wang, H. Song, I. Szabó, G. Czako, H. Guo and M. Yang, *J. Phys. Chem. Lett.*, 2016, **7**, 3322.
- 31 R. Conte, C. Qu and J. M. Bowman, *JCTC*, 2015, **11**, 1631.
- 32 A. Aguado, P. Barragan, R. Prossimi, G. Delgado-Barrio, P. Villarreal and O. Roncero, *J. Chem. Phys.*, 2010, **133**, 024306.
- 33 C. Sanz-Sanz, O. Roncero, M. Paniagua and A. Aguado, *J. Chem. Phys.*, 2013, **139**, 184302.
- 34 C. Sanz-Sanz, A. Aguado, O. Roncero and F. Naumkin, *J. Chem. Phys.*, 2015, **143**, 234303.
- 35 F. O. Ellison, *J. Am. Chem. Soc.*, 1963, **85**, 3540.
- 36 F. O. Ellison, N. T. Huff and J. C. Patel, *J. Am. Chem. Soc.*, 1963, **85**, 3544.
- 37 k. Farah, F. Muller-Plathe and M. C. Bohm, *Chem. Phys. Chem.*, 2012, **13**, 1127–1151.
- 38 A. Aguado, C. Suarez and M. Paniagua, *J. Chem. Phys.*, 1994, **101**, 4004.
- 39 C. Tablero, A. Aguado and M. Paniagua, *J. Chem. Phys.*, 1999, **110**, 7796.
- 40 F. Jensen and P. Norrby, *Theor. Chem. Acc.*, 2003, 109:1–7.
- 41 A. Aguado, C. Tablero and M. Paniagua, *Comput. Physics Commun.*, 1998, **108**, 259.
- 42 A. Aguado and M. Paniagua, *J. Chem. Phys.*, 1992, **96**, 1265.

- 43 A. J. Stone, *The theory of intermolecular forces*, Oxford University Press, New York, 2002.
- 44 A. Dorta-Urra, A. Zanchet, O. Roncero and A. Aguado, *J. Chem. Phys.*, 2015, **142**, 154301.
- 45 A. Zanchet, O. Roncero and N. Bulut, *Phys. Chem. Chem. Phys.*, 2016, **18**, 11391.
- 46 M. Karplus, R. N. Porter and R. D. Sharma, *J. Chem. Phys.*, 1965, **43**, 3259.
- 47 R. D. Levine and R. B. Bernstein, *Molecular Reaction Dynamics and Chemical Reactivity*, Oxford University Press, 1987.
- 48 R. A. Marcus, *J. Chem. Phys.*, 1952, **20**, 352.
- 49 R. A. Marcus, *J. Chem. Phys.*, 1952, **20**, 355.
- 50 J. F. E. Croft and J. L. Bohn, *Phys. Rev. A*, 2014, **89**, 012714.
- 51 U. Lourderaj, K. Park and W. L. Hase, *Int. Rev. Phys. Chem.*, 2008, **27**, 361.
- 52 D. Townsend, S. A. Lahankar, S. K. Lee, S. D. Chambreau, A. G. Suits, X. Zhang, J. Rheinecker, L. B. Harding and J. M. Bowman, *Science*, 2004, **306**, 1158.
- 53 J. Bowman and B. C. Shepler, *Annu. Rev. Phys. Chem.*, 2011, **62**, 531.
- 54 I. R. Craig and D. E. Manolopoulos, *J. Chem. Phys.*, 2004, **121**, 3368.
- 55 I. R. Craig and D. E. Manolopoulos, *J. Chem. Phys.*, 2005, **122**, 084106.
- 56 Y. V. Suleimanov, R. Colleparado-Guevara and D. E. Manolopoulos, *J. Chem. Phys.*, 2011, **134**, 044131.
- 57 Y. V. Suleimanov, F. J. Aoiz and H. Guo, *J. Phys. Chem. A*, 2016, **120**, 8488.
- 58 G. A. Voth, D. Chandler and W. H. Miller, *J. Chem. Phys.*, 1989, **91**, 7749.
- 59 E. Geva, Q. Shi and G. A. Voth, *J. Chem. Phys.*, 2001, **115**, 9209.
- 60 S. Gómez-Carrasco, L. González-Sánchez, A. Aguado, M. Paniagua, O. Roncero, M. L. Hernández and J. M. Alvaríño, *Chem. Phys. Lett.*, 2004, **383**, 25.
- 61 S. Gómez-Carrasco, L. González-Sánchez, A. Aguado, O. Roncero, J. M. Alvaríño, M. L. Hernández and M. Paniagua, *J. Chem. Phys.*, 2004, **121**, 4605.
- 62 S. Gómez-Carrasco, O. Roncero, L. González-Sánchez, M. L. Hernández, J. M. Alvaríño, M. Paniagua and A. Aguado, *J. Chem. Phys.*, 2005, **123**, 114310.
- 63 V. Sivakumaran, D. Hölscher, T. Dillon and J. N. Crowley, *Phys. Chem. Chem. Phys.*, 2003, **5**, 4821.